

Mid-latitude net precipitation decreased with Arctic warming during the Holocene

Cody C. Routson^{1*}, Nicholas P. McKay¹, Darrell S. Kaufman¹, Michael P. Erb¹, Hugues Goosse², Bryan N. Shuman³, Jessica R. Rodysill⁴ & Toby Ault⁵

The latitudinal temperature gradient between the Equator and the poles influences atmospheric stability, the strength of the jet stream and extratropical cyclones^{1–3}. Recent global warming is weakening the annual surface gradient in the Northern Hemisphere by preferentially warming the high latitudes⁴; however, the implications of these changes for mid-latitude climate remain uncertain^{5,6}. Here we show that a weaker latitudinal temperature gradient—that is, warming of the Arctic with respect to the Equator—during the early to middle part of the Holocene coincided with substantial decreases in mid-latitude net precipitation (precipitation minus evapotranspiration, at 30° N to 50° N). We quantify the evolution of the gradient and of mid-latitude moisture both in a new compilation of Holocene palaeoclimate records spanning from 10° S to 90° N and in an ensemble of mid-Holocene climate model simulations. The observed pattern is consistent with the hypothesis that a weaker temperature gradient led to weaker mid-latitude westerly flow, weaker cyclones and decreased net terrestrial mid-latitude precipitation. Currently, the northern high latitudes are warming at rates nearly double the global average⁴, decreasing the Equator-to-pole temperature gradient to values comparable with those in the early to middle Holocene. If the patterns observed during the Holocene hold for current anthropogenically forced warming, the weaker latitudinal temperature gradient will lead to considerable reductions in mid-latitude water resources.

The response of mid-latitude climate to Arctic warming is poorly understood, in part because of a lack of long-term observational data⁷. There is evidence that the strength of the latitudinal temperature gradient (LTG) influences the position, strength and meridionality of mid-latitude jet streams and storm tracks (Fig. 1)^{1,2,8,9}. Connections between the LTG and the mid-latitudes, however, may be nonlinear⁶, and attribution of recent changes in mid-latitude climate to Arctic warming remains a topic of active research⁵. A better understanding of links between Arctic amplification, the LTG and hemispheric circulation would have important implications for characterizing future variability in the mid-latitude hydroclimate.

Mid-latitude weather is largely shaped by extratropical cyclones, which form in regions of maximum baroclinic instability related to the LTG^{1,10}. One hypothesis supported by theory, observations and climate models is that Arctic warming weakens the LTG and reduces zonal mid-latitude westerly winds through the thermal wind relationship^{3,8,11,12}. The weakened LTG reduces the baroclinic potential energy that fuels storm systems, reducing mid-latitude cyclone frequency and intensity^{3,10}, and thus reducing annual net precipitation at mid-latitudes.

Palaeoclimate archives spanning the Holocene provide an opportunity to evaluate the impact of Arctic warming on the LTG and mid-latitude hydroclimates. Some model results suggest that annual LTG changes, driven annually by obliquity and seasonally by precession, would have favoured a Holocene trend towards increasing mid-to high-latitude storm activity³. Annual insolation peaked around

10,000 years ago (10 ka) in the Arctic, with maximum warming occurring about 7 ka (ref. ¹³). Insolation and temperatures have subsequently declined faster at high latitudes than at the Equator (Extended Data Fig. 1a)¹⁴, providing a natural baseline for assessing the relationship between the evolution of the surface LTG and mid-latitude hydroclimates.

In this study, we examine an extensive dataset of multi-proxy time series for the Holocene climate (Fig. 2). We explore the evolution of the LTG at three temporal scales from different but temporally overlapping datasets: the past 100 years (ref. ¹⁵), 2,000 years (ref. ¹⁶) and 10,000 years. We apply the new global compilation of 2,000-year palaeotemperature records from PAGES 2k¹⁶ to bridge between instrumental data and Holocene-long temperature reconstructions. We compare the Holocene LTG evolution with that of mid-latitude hydroclimate between 30° N and 50° N, a region that is strongly influenced by extratropical cyclones and that encompasses extensive dry-land farming and large population centres vulnerable to hydroclimate change. We then use an ensemble of mid-Holocene (6 ka) PMIP3 simulations to explore the mechanistic framework and seasonality of the changes, and to compare with the proxy data.

Gridded instrumental TS4.01 data¹⁵ from the Climatic Research Unit (CRU) show that historical LTGs have weakened over the past century by about 0.02 °C per degree of latitude (Extended Data Fig. 2a). The LTGs derived from the PAGES 2k network show recent LTG reductions, consistent with the instrumental observations, and they place the historical trend within a millennial-scale context (Extended Data Fig. 2b).

The Holocene analysis is focused on the postglacial period starting at 10 ka when Northern Hemisphere ice-sheet area had diminished to 25% of its full-glacial extent, and global atmospheric CO₂ concentration (265 ppm) and mean surface temperature reached or exceeded preindustrial values (summarized by ref. ¹⁷). The Laurentide Ice Sheet persisted until about 7 ka (ref. ¹⁸) and probably affected temperature and circulation regionally. Because of this, and because the spatial coverage of proxy sites is insufficient to detect spatial variability at fine scales, we focus our analysis on zonal averages.

Our Holocene temperature analysis uses 236 records from 219 sites including 16 proxy types collected from six archive types (Fig. 2a; Supplementary Table 1). Archive types include lake sediment ($n = 109$), marine sediment ($n = 116$), ice cores ($n = 3$), peat bogs ($n = 3$), speleothems ($n = 2$) and tree rings ($n = 3$). Alkenones and Mg/Ca are the dominant proxies for sea-surface temperature, whereas pollen- and chironomid-based reconstructions dominate the terrestrial temperature proxies. Temporal availability of temperature records is relatively uniform between 8 ka and 2 ka, with the maximum number of records available at about 5 ka. Sensitivity tests with instrumental and model data (see Methods) show that our network accurately represents Northern Hemisphere temperature variability. The 72 mid-latitude hydroclimate records from 68 sites include five archive types (lake sediment ($n = 58$), marine sediment ($n = 2$), lagoon sediment ($n = 1$), peat

¹School of Earth and Sustainability, Northern Arizona University, Flagstaff, AZ, USA. ²Université Catholique de Louvain, Earth and Life Institute, Georges Lemaître Center for Earth and Climate Research, Louvain-la-Neuve, Belgium. ³Roy J. Shlemon Center for Quaternary Studies, Department of Geology and Geophysics, University of Wyoming, Laramie, WY, USA. ⁴Florence Bascom Geoscience Center, US Geological Survey, Reston, VA, USA. ⁵Department of Earth and Atmospheric Sciences, Cornell University, Ithaca, NY, USA. *e-mail: cody.routson@nau.edu

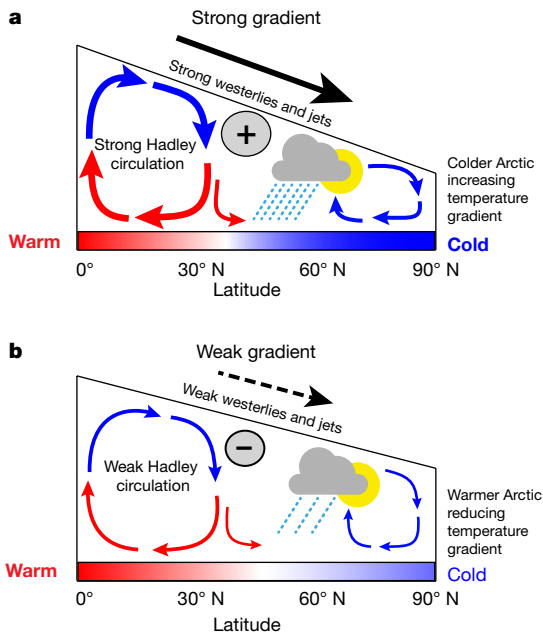


Fig. 1 | Conceptual diagram. **a**, Cold high-latitude temperatures lead to a strong temperature gradient between the Equator and the pole, a stronger subtropical jet, and enhanced mid-latitude moisture transport and net precipitation. **b**, Warming the high latitudes reduces the LTG, and is coincident with weaker Hadley circulation, weaker westerly jets, and decreased mid-latitude moisture transport and net precipitation.

bogs ($n = 4$) and speleothems ($n = 7$)) and 17 proxy types (Fig. 2b; Supplementary Table 2). Dominant proxy types include pollen, lake-level stratigraphy, oxygen isotopes and diatoms. Monsoon records were excluded from the hydroclimate analysis to help to isolate the influence of the LTG on large-scale circulation and precipitation.

On the basis of the original authors' interpretations, 45% of the temperature records represent mean-annual conditions, 48% summer and 7% winter. Mid-latitude hydroclimate records are 54% annual, 3% summer, 15% winter, 20% spring or fall, and 8% unspecified. For sites that include both season-specific and mean-annual reconstructions, the annual series was used. However, the mixture of seasonality influences our interpretations to some extent. We assume that over centennial to millennial timescales, temperature changes represented by different proxy types, including surface air, ocean surface and lake surface temperatures, generally co-vary, and we combine them in the following analysis.

Holocene temperature histories for the Northern Hemisphere differed considerably by latitude (Fig. 3). Peak warmth in the polar region (70° N to 90° N, Fig. 3a) occurred in the earliest Holocene, followed by a Holocene cooling trend. The greater variability reflects the limited number of records ($n = 20$) contributing to the polar composite. The high-latitude (50° N to 70° N, Fig. 3b) composite integrates 103 records. Holocene peak warmth occurred at about 7 ka. Later high-latitude peak warming may reflect the persistent influence of ice sheets, although the polar region had an earlier peak warming. Gradual cooling dominated the high latitudes after about 6 ka. The mid-latitude composite (30° N to 50° N, $n = 65$, Fig. 3c) warmed to about 8 ka followed by cooling. Low-latitude (10° N to 30° N, $n = 22$, Fig. 3d) and equatorial (10° S to 10° N, $n = 26$, Fig. 3e) temperatures were stable or warmed slightly over the past 10 ka.

Holocene LTGs (Fig. 3f) were weakest in the early to middle Holocene, when polar and high-latitude temperature anomalies were warmer (Fig. 3a,b) relative to the low latitudes (Fig. 3d,e). Proxy calibrations may underestimate the amplitude of Holocene temperature change (for example ref. ¹⁹); however, three methods for calculating the LTG (see Methods) all show that the LTG strengthened after the middle Holocene (Fig. 3f). Stable Holocene equatorial temperatures

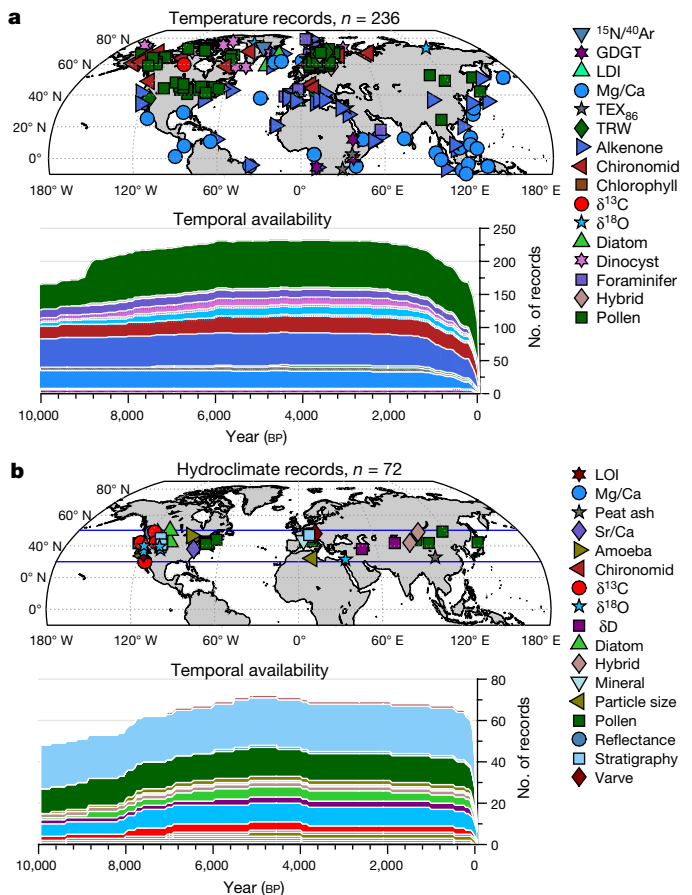


Fig. 2 | Spatial and temporal distribution of Holocene proxy records.

a, Proxy temperature records. **b**, Mid-latitude (30° N to 50° N) proxy hydroclimate records. Abbreviations for proxy types include: ratio of nitrogen-15 isotopes/argon-40 isotopes ($^{15}\text{N}/^{40}\text{Ar}$), glycerol dialkyl glycerol tetraethers (GDGT), long-chain diol index (LDI), tetraether index of 86 carbons (TEX₈₆), magnesium/calcium ratio (Mg/Ca), tree-ring width (TRW), carbon-13 isotopes ($\delta^{13}\text{C}$), oxygen-18 isotopes ($\delta^{18}\text{O}$), loss on ignition (LOI), ash content of peat (peat ash), ratio of strontium and calcium (Sr/Ca), deuterium isotopes of leaf wax (δD), and records composed of two or more proxy types (hybrid)²⁹. The maps were generated using code and associated data from ref. ³⁰. A list of sites with metadata, including references for each record, is in Supplementary Tables 1 and 2.

largely constrained the competing influence of tropical warming on the LTG and circulation (summarized by ref. ¹). The millennial-scale LTG trend (different from zero with $P < 0.0001$) tracks changes in the annual latitudinal insolation gradient (Fig. 3g), which we hypothesize was the primary driver of Holocene LTG changes.

Similar to the LTG, mid-latitude net precipitation exhibits a strong Holocene trend. The driest mid-latitude conditions occurred in the early to middle Holocene, followed by a Holocene-length wetting trend (Fig. 3h). Hydroclimate records published in calibrated units (for example, mm yr^{-1} , $n = 15$) indicate an average increase in annual net precipitation of 145 mm (93–187 mm, 5%–95% confidence interval, CI) since 8 ka, and 272 mm (130–312 mm) since about 10 ka. For the region best represented by the calibrated records (mid-latitude North America where annual precipitation equals 500–1,300 mm), the changes are equivalent to an increase of 11–29% in annual precipitation since 8 ka. Regression (Extended Data Fig. 3) indicates that the change corresponds to a net precipitation increase of 16.8 ± 7 mm per decrease of 0.01 W m^{-2} per degree of latitude in the annual latitudinal insolation gradient after the ice-sheet effect diminishes at about 8 ka. Early Holocene amplification of the dryness may be attributed to ice-sheet effects²⁰.

We used a PMIP3 climate model ensemble to test the hypothesis that a weaker LTG reduces mid-latitude rainfall (Fig. 1). The mid-Holocene

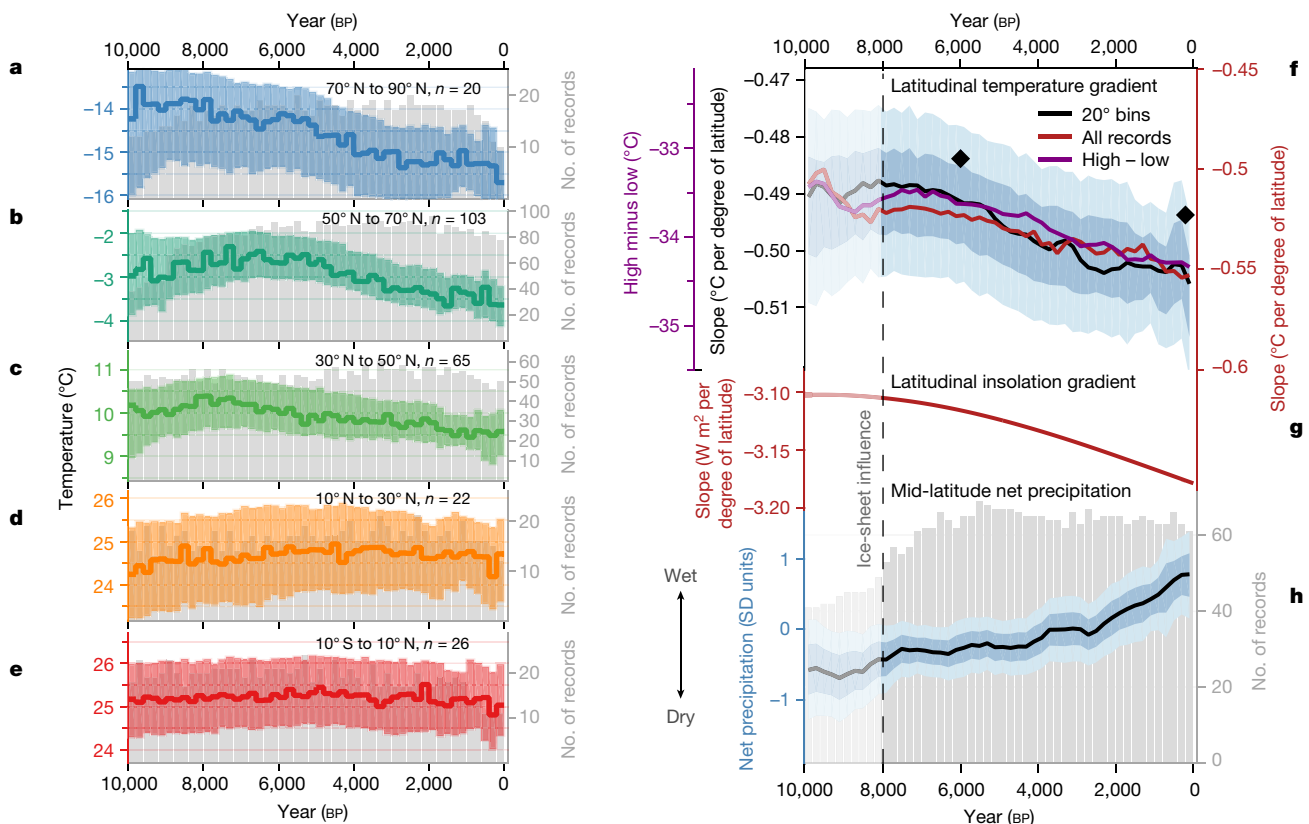


Fig. 3 | Northern Hemisphere latitudinal climate. **a–e**, Temperature composites by latitude. The numbers of contributing records are shown in grey (200-year bins). Temperature composites are all displayed on the same scale, with each *y* axis spanning 3 °C. Shading represents the 95% bootstrapped uncertainties, which integrate age and calibration uncertainty estimates (see Methods). The Holocene composites show little long-term change in the equatorial regions, and greater low-frequency variability and trends in the middle to high latitudes. **f**, LTG in the Northern Hemisphere, calculated through three different methods including regression across temperatures averaged into 20° zonal bands (black), regression on all records (red), and high latitudes minus low latitudes (purple). The LTG estimates have been smoothed with a three-bin (600-year) moving window for comparison. Diamonds show the

PMIP3 multi-model median for the simulated annual LTG at 6 ka and preindustrial, calculated using regression across 20° latitudinal averaged temperatures (black). **g**, Annual latitudinal insolation gradient for the Northern Hemisphere. **h**, Standardized, average mid-latitude (30° N to 50° N) net precipitation, with the number of contributing records in grey (200-year bins). Shading in **f** and **h** represents the one- and two-standard deviation sample, age and calibration bootstrapped uncertainty intervals (see Methods). The vertical dashed line at 8 ka in **f–h** shows when the Laurentide Ice-Sheet area and potential influence on circulation was largely reduced (Extended Data Fig. 3)¹⁸. The weakest temperature gradients in the early to middle Holocene correspond to the period of maximum Holocene aridity.

(6 ka) minus preindustrial mean of 12 models shows that the LTG change was 0.011 (95% CI 0.003–0.017) °C per degree of latitude. This compares with the LTG change of 0.015 (95% CI 0.004–0.031) °C per degree of latitude calculated from the palaeotemperature dataset for 6 ka. The modelled 6 ka simulations show that the decreased LTG is associated with reduced Hadley circulation, reduced jet-stream strength and reduced large-scale, mid-latitude precipitation (Fig. 4a,b). The large-scale component of precipitation reflects precipitation from large-scale convergence and lifting, and partially excludes monsoon-related rainfall. This allows for a more analogous comparison with the hydroclimate proxy network, which excludes monsoon records. If total precipitation or precipitation–evaporation is examined instead (Extended Data Figs. 4g,i, and 5c), the relationship persists for at least half of the models.

We interpret the seasonality of circulation and precipitation change as follows. Annual high-latitude insolation was increased during the early to middle Holocene but was especially enhanced in summer (Extended Data Fig. 1)¹⁴. The PMIP3 simulations show reduced jet-stream strength and reduced mid-latitude, large-scale precipitation throughout the year, with the largest anomalies in summer (Extended Data Fig. 4). The largest summertime response is congruent with recent work that shows that changes in the summer LTG have a strong impact on summer cyclogenesis²¹, and congruent with the tendency of many proxies to track summer conditions more closely (for example ref. 22;

see Methods). We hypothesize that enhanced high-latitude summer insolation led to enhanced warming both at the surface and aloft. Warmer summers led to reduced sea-ice extent, a longer ice-free season and thinner sea ice, increasing the heat fluxes between the ocean and atmosphere that propagated into the cold season as observed during recent Arctic amplification⁴ and in Holocene model simulations²³. Arctic warming would have reduced the LTG, subsequently reducing the strength and frequency of storms for much of the year, and thereby reducing annual net precipitation at mid-latitudes. This mechanistic framework is consistent with model results showing that a strengthening LTG driven by obliquity and seasonally by precession would favour a Holocene trend towards increasing mid- to high-latitude storm activity³.

Several alternative hypotheses have been proposed about Holocene circulation and potential links to changes in temperature and insolation gradients^{9,24}. For example, changes in the insolation gradient have been linked to stronger wintertime westerlies over Europe⁹ and weaker summertime westerly flow²⁴. A predominantly positive mid-Holocene winter North Atlantic Oscillation has been suggested^{25,26}, and a cooler tropical Pacific Ocean may have caused North American aridity²⁷. These hypotheses are still debated, and there is no clear consensus on Holocene circulation changes^{24,28}. Nevertheless, the reduced mid-latitude net precipitation inferred from the proxy records (Fig. 3h), and the reduced westerlies and precipitation shown by the PMIP3 models

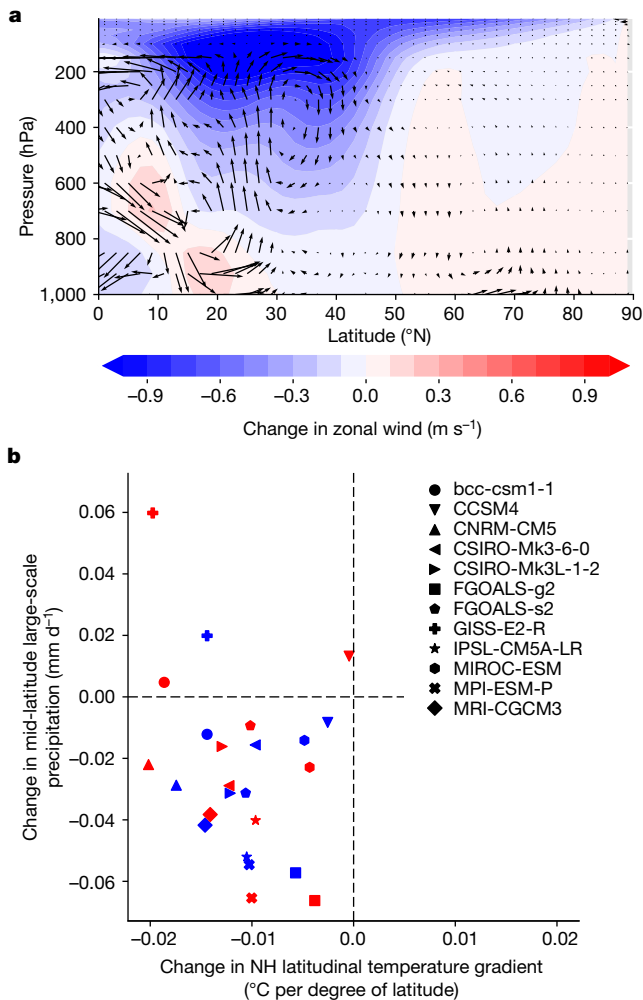


Fig. 4 | Mid-Holocene (6 ka) PMIP3 modelled circulation and large-scale precipitation anomalies relative to preindustrial. a, Nine-model mean circulation anomalies showing annual-mean changes in meridional and vertical motion (vectors; the scale for vertical motion has been increased to aid viewing) and zonal winds (contours; m s^{-1}). Anomalies show weakened annual Hadley circulation and reduced zonal wind speed during the mid-Holocene. **b**, Relation between the LTG and large-scale precipitation (that is, precipitation corresponding to large-scale convergence and lifting) for 12 PMIP3 models. Blue symbols indicate zonal-mean values, with the temperature gradient calculated over 10°S to 90°N , and precipitation calculated over $30^{\circ}\text{--}50^{\circ}\text{N}$. Red symbols show averages calculated using model data at proxy locations only. Negative values on the x -axis indicate a reduced LTG at 6 ka relative to preindustrial. Three models shown in **b** (CSIRO-Mk3L-1-2, FGOALS-g2 and GISS-E2-R) lacked the output fields necessary for inclusion in the multi-model means in **a** and Extended Data. NH, Northern Hemisphere.

(Fig. 4), are not consistent with stronger westerlies suggested by some of those studies.

Recent and projected warming and drying feedbacks¹² suggest an alternative hypothesis that early to middle Holocene mid-latitude aridity was caused by higher summer insolation driving enhanced evaporation, rather than by changes in storm tracks and circulation. Precipitation and evaporation-induced drying were most likely complementary, which is supported in the PMIP3 models (Extended Data Fig. 4h). The PMIP3 models indicate that mid-latitude drying ($\sim 40^{\circ}\text{--}55^{\circ}\text{N}$) was dominated by reductions in precipitation (Extended Data Fig. 5c). However, the simulated magnitude of drying is small ($<0.05 \text{ mm d}^{-1}$; Extended Data Fig. 5c) compared with the magnitudes reconstructed using the calibrated datasets ($>0.3 \text{ mm d}^{-1}$ at 6 ka; Extended Data Fig. 3b). The driest period of the Holocene coincided with cool conditions when ice sheets still persisted in the high latitudes,

indicating that circulation change was likely to be a dominant driver of aridity at that time.

In summary, the proxy climate data presented here show that a reduced early- to middle-Holocene LTG coincided with substantial decreases in mid-latitude net precipitation. More work and additional records are needed to fully resolve regional and sub-regional variability; however, an ensemble of PMIP3 models is consistent with the proxy evidence and shows a weaker mid-Holocene LTG corresponded with reduced jet-stream strength and reduced mid-latitude precipitation. Current and future conditions are more complex than during the Holocene because greenhouse gases are forcing a larger mean temperature change and have multiple and competing influences on circulation^{1,12}. Nevertheless, it is reasonable to assume that the relationship between the surface LTG and circulation holds, offering a framework to help in understanding the impact of atmospheric dynamics on both past and future changes.

Online content

Any methods, additional references, Nature Research reporting summaries, source data, statements of data availability and associated accession codes are available at <https://doi.org/10.1038/s41586-019-1060-3>.

Received: 7 July 2017; Accepted: 22 January 2019;
Published online 27 March 2019.

- Shaw, T. A. et al. Storm track processes and the opposing influences of climate change. *Nat. Geosci.* **9**, 656–664 (2016).
- Semmler, T. et al. Seasonal atmospheric responses to reduced Arctic sea ice in an ensemble of coupled model simulations. *J. Clim.* **29**, 5893–5913 (2016).
- Jackson, C. S. & Broccoli, A. J. Orbital forcing of Arctic climate: mechanisms of climate response and implications for continental glaciation. *Clim. Dyn.* **21**, 539–557 (2003).
- Serreze, M. C. & Barry, R. G. Processes and impacts of Arctic amplification: a research synthesis. *Global Planet. Change* **77**, 85–96 (2011).
- Barnes, E. A. & Screen, J. A. The impact of Arctic warming on the midlatitude jet-stream: can it? has it? will it? *WIREs Clim. Change* **6**, 277–286 (2015).
- Overland, J. E. et al. Nonlinear response of mid-latitude weather to the changing Arctic. *Nat. Clim. Chang.* **6**, 992–999 (2016).
- Vihma, T. Effects of Arctic sea ice decline on weather and climate: a review. *Surv. Geophys.* **35**, 1175–1214 (2014).
- Francis, J. A. & Vavrus, S. J. Evidence for a wavier jet stream in response to rapid Arctic warming. *Environ. Res. Lett.* **10**, 014005 (2015).
- Davis, B. A. S. & Brewer, S. Orbital forcing and role of the latitudinal insolation/temperature gradient. *Clim. Dyn.* **32**, 143–165 (2009).
- Chang, E. K. M., Lee, S. & Swanson, K. L. Storm track dynamics. *J. Clim.* **15**, 2163–2183 (2002).
- Son, S.-W. & Lee, S. The response of westerly jets to thermal driving in a primitive equation model. *J. Atmos. Sci.* **62**, 3741–3757 (2005).
- Seager, R. et al. Dynamical and thermodynamical causes of large-scale changes in the hydrological cycle over North America in response to global warming. *J. Clim.* **27**, 7921–7948 (2014).
- Marcott, S. A., Shakun, J. D., Clark, P. U. & Mix, A. C. A reconstruction of regional and global temperature for the past 11,300 years. *Science* **339**, 1198–1201 (2013).
- Berger, A. & Loutre, M. F. Insolation values for the climate of the last 10 million years. *Quat. Sci. Rev.* **10**, 297–317 (1991).
- Harris, I., Jones, P. D., Osborn, T. J. & Lister, D. H. Updated high-resolution grids of monthly climatic observations – the CRU TS3.10 Dataset. *Int. J. Climatol.* **34**, 623–642 (2014).
- PAGES2k Consortium. A global multiproxy database for temperature reconstructions of the Common Era. *Sci. Data* **4**, 170088 (2017).
- Shakun, J. D. et al. Global warming preceded by increasing carbon dioxide concentrations during the last deglaciation. *Nature* **484**, 49–54 (2012).
- Carlson, A. E. et al. Rapid early Holocene deglaciation of the Laurentide ice sheet. *Nat. Geosci.* **1**, 620–624 (2008).
- Huang, S. P., Pollack, H. N. & Shen, P.-Y. A late Quaternary climate reconstruction based on borehole heat flux data, borehole temperature data, and the instrumental record. *Geophys. Res. Lett.* **35**, L13703 (2008).
- Shuman, B. & Plank, C. Orbital, ice sheet, and possible solar controls on Holocene moisture trends in the North Atlantic drainage basin. *Geology* **39**, 151–154 (2011).
- Coumou, D., Lehmann, J. & Beckmann, J. The weakening summer circulation in the Northern Hemisphere mid-latitudes. *Science* **348**, 324–327 (2015).
- Marsicek, J., Shuman, B. N., Bartlein, P. J., Shafer, S. L. & Brewer, S. Reconciling divergent trends and millennial variations in Holocene temperatures. *Nature* **554**, 92–96 (2018).
- Renssen, H. et al. Simulating the Holocene climate evolution at northern high latitudes using a coupled atmosphere–sea ice–ocean–vegetation model. *Clim. Dyn.* **24**, 23–43 (2005).

24. Mauri, A., Davis, B. A. S., Collins, P. M. & Kaplan, J. O. The influence of atmospheric circulation on the mid-Holocene climate of Europe: a data–model comparison. *Clim. Past* **10**, 1925–1938 (2014).
25. Rimbu, N., Lohmann, G., Kim, J.-H., Arz, H. W. & Schneider, R. Arctic/North Atlantic Oscillation signature in Holocene sea surface temperature trends as obtained from alkenone data. *Geophys. Res. Lett.* **30**, 1280 (2003).
26. Wanner, H. et al. Mid- to Late Holocene climate change: an overview. *Quat. Sci. Rev.* **27**, 1791–1828 (2008).
27. Shin, S.-I., Sardeshmukh, P. D., Webb, R. S., Oglesby, R. J. & Barsugli, J. J. Understanding the Mid-Holocene climate. *J. Clim.* **19**, 2801–2817 (2006).
28. Gladstone, R. M. et al. Mid-Holocene NAO: A PMIP2 model intercomparison. *Geophys. Res. Lett.* **32**, L16707 (2005).
29. Chen, F. et al. Holocene moisture evolution in arid central Asia and its out-of-phase relationship with Asian monsoon history. *Quat. Sci. Rev.* **27**, 351–364 (2008).
30. Pawlowicz, R. *M_Map: A Mapping Package for MATLAB* (2018).

Acknowledgements Funding for this research was provided by the Science Foundation Arizona Bisgrove Scholar award (BP 0544-13), the National Science Foundation (AGS-1602105 and EAR-1347221), and the State of Arizona Technology and Research Initiative Fund administered by the Arizona Board of Regents. We acknowledge support by the USGS Climate and Land Use Program (any use of trade, product or firm names is for descriptive purposes only and does not imply endorsement by the US government). H.G. is Research Director at the Fonds de la Recherche Scientifique–FNRS (Belgium). We thank D. Coumou and USGS reviewers M. Robinson and T. Cronin for comments on the manuscript. This work benefited from the new compilation of proxy temperature records for the past 2,000 years that was led by the Past Global Changes (PAGES) project, and from discussions with colleagues at PAGES-sponsored workshops. We thank all original data

contributors who made their data available. We also thank the leaders of, and the many contributors to, the data compilations that were integrated in this study.

Reviewer information *Nature* thanks Matthew Kirby, Fredrik Charpentier Ljungqvist and the other anonymous reviewer(s) for their contribution to the peer review of this work.

Author contributions C.C.R. conceived and designed the study with contributions to the conceptual framework from N.P.M., H.G., D.S.K. and T.A. C.C.R. compiled the dataset with data contributions from J.R.R. and B.N.S. N.P.M. built the database framework. C.C.R. and B.N.S. conducted the proxy analyses with input from N.P.M., D.S.K. and H.G. M.P.E. conducted the PMIP3 model analyses. C.C.R. and D.S.K. wrote the paper with input from the other authors.

Competing interests The authors declare no competing interests.

Additional information

Extended data is available for this paper at <https://doi.org/10.1038/s41586-019-1060-3>.

Supplementary information is available for this paper at <https://doi.org/10.1038/s41586-019-1060-3>.

Reprints and permissions information is available at <http://www.nature.com/reprints>.

Correspondence and requests for materials should be addressed to C.C.R.

Publisher's note: Springer Nature remains neutral with regard to jurisdictional claims in published maps and institutional affiliations.

© The Author(s), under exclusive licence to Springer Nature Limited 2019

METHODS

Holocene dataset. Proxy records for Holocene temperature were selected that span a minimum duration of 4,000 years since 10 ka, with an average sample resolution finer than 400 years and age control points at least every ~3,000 years. Records were compiled from datasets in refs. ^{13,29,31,32}, NOAA-WDS Palaeoclimatology and PANGAEA data libraries, in addition to individual records not previously stored in public archives (Supplementary Tables 1 and 2). Temperature records were compiled between 10° S and 90° N, and only records previously calibrated to temperature units (degrees) were used in this analysis (that is, we did not include uncalibrated temperature records).

Holocene hydroclimate patterns were characterized using proxy records that met the above age and resolution criteria. We included both calibrated records (for example, mm yr⁻¹ of precipitation) and uncalibrated records (for example, $\delta^{18}\text{O}$ of lacustrine calcite) that were interpreted by the original authors as sensitive to changes in hydroclimate such as precipitation, precipitation minus evaporation, lake level and drought severity. Mid-latitude hydroclimate patterns were calculated from sites located between 30° N and 50° N. Monsoon records were excluded from the analysis to isolate the trends in hydroclimate sourced primarily from extratropical cyclones and associated flow of westerly winds.

Data normalization and binning. Methods for analysing the different datasets, including instrumental temperature¹⁵, 2,000-year (2k) temperature¹⁶, Holocene temperature and Holocene hydroclimate, are summarized in Supplementary Tables 1 and 2. MATLAB code used to map the dataset (Fig. 2) and compute composites (Fig. 3) was modified from ref. ³³. The mean for 10–0 ka (or the entire record-length mean if shorter) was subtracted from each record. Hydroclimate proxies were also normalized to have variance of ± 1 s.d. over the period 10–0 ka or over the entire record length if shorter, so that relative hydroclimate changes can be compared between climatologically diverse regions (for example, ref. ³⁴).

Holocene temperature and hydroclimate records were binned to 200-year resolution by averaging the measurements within 200-year intervals. 2k temperature records¹⁶ were binned to 20-year resolution, and historic CRU TS4.01 data¹⁵ were averaged to annual (1-year) resolution.

Producing composites. Composite time series were used to characterize Holocene temperature changes and mid-latitude net precipitation. Temperature records were composited across five 20° zonal bands between 10° S and 90° N. Mid-latitude hydroclimate records were composited between 30° N and 50° N. Composites were generated using an equal-area grid (for example Extended Data Fig. 6f) to reduce the influence of clustered sites on the composites, especially at the higher latitudes. The equal-area grid was generated in MATLAB following methods developed by ref. ³⁵. Records inside each grid were averaged and then the grids were averaged. The median was used to reduce the influence of outliers.

Composite uncertainties were estimated with a bootstrap sampling approach to develop a probability distribution from the available data and associated uncertainties³⁶. Uncertainties arising from the spatial and temporal distribution of available records were characterized using sampling-with-replacement. Age uncertainties were estimated as a normal distribution with a 10% standard deviation for each sample measurement in every record. Age uncertainty was applied by multiplying the age of each sample within each record by a random number drawn from a normal distribution with a mean of 1 and a standard deviation of 0.1 in each of 500 bootstrapped iterations. A more formal treatment of the age uncertainty would require an analysis of each record's age model, which is not available for many records in the database; nonetheless, our accounting for the age uncertainty is a conservative estimation of the likely effect. Additionally, we estimate temperature calibration uncertainty as a normal distribution for each measurement with a standard deviation by proxy as follows: 1.7 °C for chironomid, 1.1 °C for alkenone, 1 °C for pollen, 0.3 °C for ice and 1.5 °C for other proxy types. Records were then composited and the above process repeated over 500 iterations to generate a probabilistic distribution of composites.

Scaling the temperature composites. Many of the Holocene temperature records were originally published as temperature anomalies rather than as absolute temperatures, which are needed to calculate hemispheric LTGs. We applied the following shingled approach, using modern CRU TS4.01 observations¹⁵ and the PAGES 2k temperature network¹⁶, to scale the overlapping mean Holocene temperature records. The largely uncalibrated 2k network data were composited by 20° zonal bands between 10° S and 90° N (Extended Data Fig. 7) and converted to temperature units by scaling the overlapping data to match the instrumental mean and variance of the CRU TS4.01 data¹⁵. The CRU TS4.01 temperatures were weighted by the cosine of latitude to account for the smaller surface area of the high-latitude bands and composited into corresponding 20° zonal bands. The mean for 500–1,500 years BP (450–1450 CE) of the individual Holocene records and the 20° zonal composites were then scaled to the overlapping mean 2k composites. Individually scaled records and scaled composites were used in separate methods for calculating the LTG as described below. The variance of the Holocene

temperature records did not require scaling because only Holocene records previously scaled to temperature units were used.

Calculating temperature gradients. Northern Hemisphere LTGs between the colder high latitudes and warmer low latitudes were calculated using three methods. The first method was applied to (1) the twentieth century using CRU TS4.01 data¹⁵, (2) the past 2,000 years using PAGES 2k temperature network¹⁶ and (3) the entire Holocene using our new compilation of Holocene-length temperature reconstructions. This method relied on weighted linear regression across temperatures composited for five 20° zonal bands between 10° S and 90° N (Fig. 3a–e and Extended Data Fig. 8a). The 20° width of each band provided enough proxy records to generate relatively stable Holocene (Fig. 3a–e) and 2k (Extended Data Fig. 7) temperature estimates, while also representing a broad meridional temperature range. Narrower bands (10° and 15° wide) were also tested but resulted in too few records to generate robust composites, especially at the highest latitudes. Simulated PMIP3 gradients (Fig. 3f) were also calculated using the above method, but no scaling was required because the model data were already in native temperature units.

The second method applied regression on the distribution of individual Holocene temperature records rather than zonal composites (Extended Data Fig. 8b). Each record was scaled to its respective latitude also using a shingling approach. First, CRU TS4.01 gridded observations¹⁵ were used to scale the PAGES 2k network¹⁶, which was then used to scale the overlapping mean of the individual Holocene records. Only Holocene records with data in the interval 500 to 1,500 BP were used so they could be scaled to the overlapping portion of the 2k network. Many of the low-resolution 2k records had insufficient overlap with the instrumental period to scale their variance using the instrumental data individually. Instead, the 2k records were composited by 20° latitude bands, and interpolation was used to calculate the latitudinal temperatures to scale the individual Holocene records based on their latitude. Specifically, the Piecewise Cubic Hermite Interpolating Polynomial algorithm in MATLAB was used to interpolate between the 20° zonal composites based on the PAGES 2k dataset. The 500 to 1,500 BP mean was used to scale the Holocene records.

Both regression-based methods applied robust, area-weighted linear regression in MATLAB. Regression was weighted by the cosine of latitude to account for the represented earth surface area to provide an area-weighted estimate of the surface thermal energy gradient³⁷. For regression across composites, the LTGs were calculated on each of the 500-bootstrapped latitudinal composite ensembles, generating a distribution of possible LTG realizations, reflecting the range of potential age, sample and calibration uncertainties.

The third method for calculating the LTG relied on the difference between high-latitude and low-latitude temperature composites⁹ rather than the slope of regression. Temperature records were composited for 50° N to 90° N to characterize high latitudes, and from 10° S to 30° N to characterize low latitudes (Extended Data Fig. 6g, h). The Holocene LTG was computed by subtracting the low-latitude composite from the high-latitude composite.

Calculating insolation gradients. Latitudinal insolation gradients (Fig. 3g) were calculated using insolation time-series data from ref. ¹⁴ output from MATLAB code from ref. ³⁸. Holocene annual insolation time-series were averaged into 20° latitudinal bands following the latitude intervals in Fig. 3a–e. We applied robust regression weighted by the cosine of latitude to calculate the latitudinal insolation slope between northern low and high latitudes following the same method that we used to calculate the evolution of the Holocene LTG on zonally averaged temperature composites.

Calibrated hydroclimate records. The small subset of hydroclimate records published in calibrated units (for example, mm yr⁻¹, $n = 15$, Supplementary Table 2) were binned into 200-year intervals, and the median value was used for the composite time series (Extended Data Fig. 3). These records are primarily located in North America and are based on pollen and stratigraphy proxy types. A regression model using the latitudinal insolation gradient, Laurentide Ice-Sheet area and an autoregressive (ar1) term (for the residuals to account for autocorrelation in the hydroclimate records) was used to estimate the magnitude of Holocene effective precipitation change as characterized by this subset of records.

Holocene climate models. To explore Holocene climate change in models, mid-Holocene (6 ka) and preindustrial (0 ka) simulations were analysed in 12 general circulation models (GCMs) from the Paleoclimate Modelling Intercomparison Project phase III (PMIP3). Compared with the preindustrial period, mid-Holocene simulations are forced by altered astronomical parameters as well as prescribed greenhouse gases. Ice sheets had already melted to their preindustrial extents, making this a good period for exploring post-glacial climate changes. Climate anomalies are explored as mid-Holocene minus preindustrial. The experimental design is described in refs. ^{39,40}.

The 12 models analysed in this research are the models for which the necessary outputs were readily accessible, and are listed as follows: bcc-csm1-1, CCSM4, CNRM-CM5, CSIRO-Mk3-6-0, CSIRO-Mk3L-1-2, FGOALS-g2, FGOALS-s2, GISS-E2-R, IPSL-CM5A-LR, MIROC-ESM, MPI-ESM-P and MRI-CGCM3.

Three models (CSIRO-Mk3L-1-2, GISS-E2-R, and FGOALS-g2) were omitted from the ensemble-mean analyses (Fig. 4a and Extended Data Figs. 4, 5) because they lacked necessary output variables.

Where models were examined individually (Fig. 4b), calculations were made using the models' original grids. For the remaining analyses, model output was regridded onto a common 2° latitude by 2.66° longitude grid, with common pressure levels for non-surface variables, to aid comparison between models.

Dataset limitations. The extensive palaeotemperature multi-proxy dataset used in this study provides a unique view into past climate variability on a hemispheric scale. Nonetheless, there are limitations inherent to proxy records, including uncertainties related to seasonality, sample density, spatial distribution, chronology, calibration and other factors that limit our interpretations.

Importantly for this analysis, most sea-surface temperature reconstructions are based on Mg/Ca and alkenones, which predominantly record growing-season temperatures (for example ref. ⁴¹), even though they are typically calibrated to annual temperatures. Warm-season bias can also occur in other proxies that are active during the summer growing season. We selected annual temperature reconstructions when available, but our temperature results have a warm-season bias⁴². As reported by the original authors, 48% of the reconstructions reflect warm-season temperatures, but this does not address warm-season biases of proxies scaled to annual temperatures.

Although our temperature database is biased towards the warm season, the impact of this bias is limited at high latitudes where the pattern of long-term summer temperature anomalies is likely to be comparable with annual anomalies. In the Arctic, summer temperature anomalies have the potential to impact annual temperatures disproportionately by controlling glacier and sea-ice extent, and the expansion of tundra over forest, which together have large impacts on long-term annual mean temperature. This phenomenon is evident in climate model simulations of the mid-Holocene, which consistently show a sustained impact of increased summer insolation on temperature anomalies into the Arctic fall and winter, despite decreases in insolation during these seasons (for example ref. ⁴³). An additional effect that can cause summer and annual temperature anomalies to co-vary is that both summer and annual high-latitude insolation decrease through the late Holocene owing to changes in obliquity (Extended Data Fig. 1a).

Individual temperature (Extended Data Fig. 6a–e) and hydroclimate (Extended Data Fig. 9h) records are also highly variable and unevenly distributed geographically (Fig. 2). The temperature dataset (as are its zonally averaged and gridded composites) is weighted towards data-rich regions of the Alaska-Yukon, North Atlantic/Fennoscandia and western Tropical Pacific. Data-poor regions reflect a combination of limited dataset generation and data accessibility. In light of data-poor regions, we conducted a set of sensitivity tests to assess the representativeness of the proxy network.

Representativeness of the proxy network relative to zonal averages. Sensitivity analyses were conducted to test whether our proxy network accurately represents the large spatial and temporal patterns addressed in this study. Gridded instrumental-based temperatures from the CRU TS4.01 0.5° dataset were used to test how well the proxy locations represent the mean temperature over the entire 20° latitudinal bands, as shown in Fig. 3a–e. Instrumental temperature data were binned to decadal resolution to better represent the long timescales integrated by the proxy records. Grid cells corresponding to the locations of proxy records were then averaged and compared with the mean of the entire latitudinal band in which they are located. The temperature proxy locations explain between 77% and 96% of the variance in the latitudinal average (Extended Data Fig. 10a–e). The mean temperatures at the proxy locations are offset (warmer or colder) compared with the latitudinal average for most zones. The effect of this offset on the calculated LTGs is minimal, however, because our zonal mean Holocene reconstructions are adjusted to the latitudinal average over the past 2 ka, which itself is scaled to instrumental observations.

The representativeness of the proxy network of the mid-latitude hydroclimate dataset was also tested using CRU TS4.01 gridded precipitation observations following the same methods as for the temperature network (Extended Data Fig. 10g). The hydroclimate proxy locations explain 78% of the variance of the latitudinal average.

In addition to the instrumental data, we also used the ensemble of PMIP3 models to assess how well our proxy network represents the latitudinal bands. The change in mid-Holocene minus preindustrial temperatures for the five latitude bands was calculated for both the proxy locations and the latitudinal averages in 12 models (Extended Data Fig. 10). The proxy locations explain 93% of the variance in the latitudinal averages of mid-Holocene minus preindustrial changes. We also calculated the LTGs and precipitation changes using the proxy locations in the mid-Holocene (6 ka) runs of PMIP3 models. The mean of the proxy sites is strikingly similar to the mean of the full field, with increasing precipitation associated with a stronger LTG (Fig. 4b).

Finally, correlation analysis using the proxy records was also used to assess whether the hydroclimate proxy network accurately represents the broad region of interest (Extended Data Fig. 10h). New composites with iteratively smaller sample sizes were generated by randomly removing 1–71 records from the hydroclimate composite over 20,000 iterations. Correlation strength between the composites and the final composite drops quickly as sample size decreases below about 40 hydroclimate records, indicating that our sample network ($n = 72$) is sufficient to capture the broad temporal patterns addressed in this paper.

Effect of standardizing the moisture records. Most Holocene hydroclimate records are published using their native proxy-value units (for example, lake level) and not converted to units of precipitation or evaporation amount (for example, mm yr^{-1}). To integrate and summarize the hydroclimate proxy records, we converted them into relative units by subtracting the Holocene mean (0–10 ka), or subtracting the full-record-length mean if shorter, and dividing by the standard deviation calculated over the same interval. To evaluate the effect of standardization, we applied the same standardization methodology to gridded instrumental observations of precipitation from CRU TS4.01 (Extended Data Fig. 10g). The results show that the standardized mid-latitude average explains 98% of the variance of the mid-latitude average in native units (mm month^{-1}), demonstrating that standardized hydroclimate time series closely track the temporal variability and the magnitude of change.

In addition to the standardized records, our proxy dataset includes 15 moisture records that were reported in precipitation units (mm yr^{-1}) (Supplementary Table 2). These records were used to quantify the absolute magnitude of the Holocene wetting trend in areas that they represent (predominantly North America).

Palaeodata–model comparison. Simulations of mid-Holocene (6 ka) climate by the PMIP3 model ensemble are largely consistent with the proxy data for this time slice. In response to increased obliquity at 6 ka, annual-mean insolation was increased at the poles and decreased at the Equator (Extended Data Fig. 1a). A Northern Hemisphere spring perihelion additionally modified the seasonal insolation cycle (Extended Data Fig. 1b). The PMIP3 multi-model mean response to this forcing shows a weaker meridional temperature gradient compared with preindustrial (Extended Data Fig. 5a, b), decreased zonal wind strength (Fig. 4a), reduced Hadley circulation (Fig. 4a) and reductions in mid-latitude net precipitation (Extended Data Fig. 5c). The reduction in net precipitation is due to changes in both precipitation and evaporation. In the models, precipitation can also be separated into large-scale precipitation (that is, precipitation changes due to large-scale convergence or lifting) and convective precipitation (that is, precipitation related to smaller-scale processes, which must be parameterized in the models). The reduction in mid-latitude precipitation is primarily in the large-scale category.

Changes in Hadley circulation shown in the models are consistent with the mechanistic framework that a stronger/weaker LTG would lead to increased/reduced meridional circulation. However, stronger Hadley circulation would potentially be a countervailing force to enhanced storm activity, leading to drier conditions on the subtropical edge of the mid-latitudes. Changes in Hadley Circulation could account for some of the variability observed amongst the mid-latitude hydroclimate records.

Below 30° N latitude, the models show a wide range of precipitation changes at 6 ka relative to preindustrial (Extended Data Fig. 5c), predominantly related to the position of the intertropical convergence zone and strength of monsoon systems. Although the changes are large at low latitudes, there is also considerable spread among the modelled responses. The magnitude of mid-latitude (30° N to 50° N) precipitation change simulated by the models is smaller than those in the proxy records. Only a small subset of the proxy records is calibrated to hydroclimate units, primarily located in North America. Nonetheless, these proxy records show an increase of 93 – 187 mm yr^{-1} in precipitation since 8 ka, whereas the model ensemble-mean suggests only an increase of ~ 4 mm yr^{-1} since 6 ka when averaged over the same locations and seasons, though larger anomalies are present regionally, during different parts of the year, or in individual models. Proxy records commonly indicate greater palaeoclimate change than those in models⁴⁴, and palaeodata–model differences have been described more generally^{42,45}, but more work is needed to resolve this data–model discrepancy.

Hydroclimate regional differences. As noted by previous work, the timing and progression of Holocene hydroclimate differed between North America and Eurasia²⁰. The dataset presented here suggests that the driest mid-latitude conditions occurred in North America ($n = 43$) during the early to middle Holocene with a gradual, nearly linear, transition from a drier to wetter environment (Extended Data Fig. 9f), whereas Eurasia ($n = 29$) had more variable hydroclimates over the Holocene (Extended Data Fig. 9g). Eurasia shows a Holocene wetting trend, but the trend is interrupted by a relatively arid interval between 4 ka and 5 ka. It is unclear to what extent these regional differences are robust in our dataset. The Eurasian composite relies on fewer records and spans a climatologically diverse

region. For example, Asia has strong monsoon systems, and although records interpreted as monsoon indicators were excluded from this analysis, the monsoon boundary was probably further north during the Holocene⁴⁶. Additional records and further analyses are needed to unravel regional and sub-regional hydroclimate variability.

Hydroclimate proxies. Individual hydroclimate proxy types ($n = 17$) in the dataset were examined to assess if different proxy types were in agreement. Holocene composites including the dominant hydroclimate proxy types: physical sediment properties (stratigraphy; $n = 23$), pollen ($n = 14$), $\delta^{18}\text{O}$ of lacustrine calcite ($n = 9$), diatom ($n = 5$) and other proxies ($n = 21$) are shown in Extended Data Fig. 9a–e. Stratigraphy records show the driest conditions between 10 ka and ~6 ka, followed by a relatively linear wetting trend. Pollen records, located both in North America and Asia, suggest that conditions were driest in the earliest Holocene with a steep wetting trend to ~7 ka. After 7 ka, pollen records suggest variable but generally increasing net precipitation through the remainder of the Holocene. Oxygen-isotope-inferred hydroclimate records, primarily from the Middle East and North America, show a trend towards wetter conditions between 10 ka and ~3 ka, then drying to the present. The five diatom records are exceptionally variable, with no clear Holocene trends. The other proxies (that is, proxy types consisting of fewer than five individual records) suggest subtle to no Holocene trends. Of the dominant proxy types included, stratigraphy and pollen records show the strongest Holocene wetting trends.

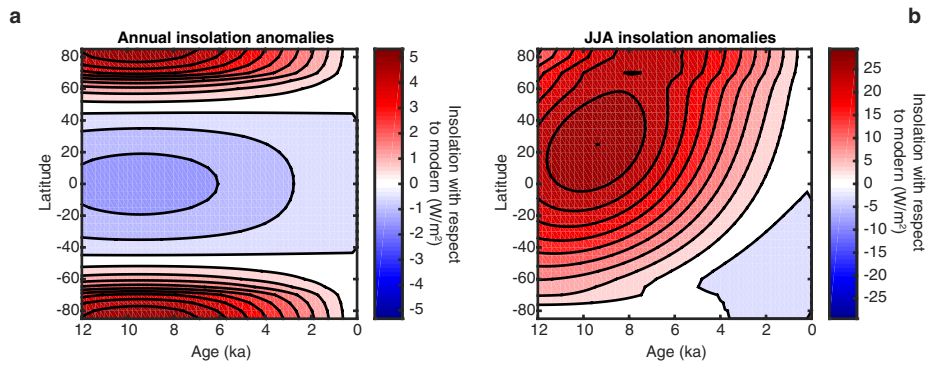
Data availability

All of the proxy and instrumental climate records that were analysed in this study are from published sources. Supplementary Tables 1 and 2 include the citations to the original publications for each of the Holocene-long temperature and hydroclimate proxy records, respectively. The proxy data and basic metadata for the time series compiled for this study from these sources are available at the World Data Service for Paleoclimatology hosted by NOAA (<https://www.ncdc.noaa.gov/paleo/study/25890>). The landing page includes links to digital versions of the primary results (time series) generated by this study, including the (1) Holocene temperature composites by latitude (Fig. 3a–e), (2) Northern Hemisphere LTG (Fig. 3f) and (3) mid-latitude net precipitation reconstruction (Fig. 3h). The proxy temperature records for the past 2,000 years were compiled by the PAGES2k Consortium¹⁶ and are available at: <https://www.ncdc.noaa.gov/paleo-search/study/21171>. The CRU instrumental data are available at <http://www.cru.uea.ac.uk/>. PMIP3 model output is available at <https://esgf-node.llnl.gov/projects/esgf-llnl/>.

Code availability

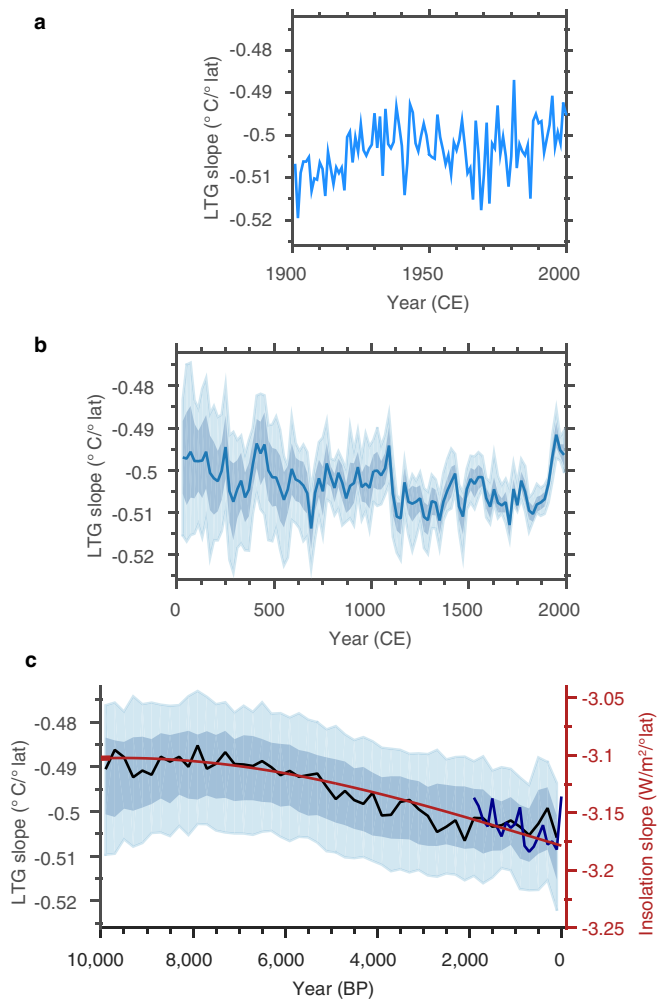
The MATLAB code (<https://www.mathworks.com/products/matlab.html>) used to create the figures in this article was modified from code developed by Emile-Geay et al.³³, which is available at https://github.com/CommonClimate/PAGES2k_phase2 under a free BSD licence.

31. Sundqvist, H. S. et al. Arctic Holocene proxy climate database—new approaches to assessing geochronological accuracy and encoding climate variables. *Clim. Past* **10**, 1605–1631 (2014).
32. Wanner, H., Solomina, O., Grosjean, M., Ritz, S. P. & Jetel, M. Structure and origin of Holocene cold events. *Quat. Sci. Rev.* **30**, 3109–3123 (2011).
33. Emile-Geay, J., McKay, N. P., Wang, J. & Anchukaitis, K. J. CommonClimate/PAGES2k_phase2 code: first public release. <https://doi.org/10.5281/zenodo.545815> (2017).
34. Shuman, B. N. & Marsicek, J. The structure of Holocene climate change in mid-latitude North America. *Quat. Sci. Rev.* **141**, 38–51 (2016).
35. Leopardi, P. C. A partition of the unit sphere into regions of equal area and small diameter. *Electron. Trans. Numer. Anal.* **25**, 309–327 (2006).
36. Boos, D. D. Introduction to the bootstrap world. *Stat. Sci.* **18**, 168–174 (2003).
37. Jain, S., Lall, U. & Mann, M. E. Seasonality and interannual variations of Northern Hemisphere temperature: Equator-to-pole gradient and ocean-land contrast. *J. Clim.* **12**, 1086–1100 (1999).
38. Huybers, P. & Eisenman, I. *Integrated summer insolation calculations*. IGBP PAGES/WDC Contribution Series 2006-079 (NOAA/NCDC Paleoclimatology Program, 2006).
39. Braconnot, P. et al. Evaluation of climate models using palaeoclimatic data. *Nat. Clim. Change* **2**, 417–424 (2012).
40. Braconnot, P. et al. The Paleoclimate Modeling Intercomparison Project contribution to CMIP5. *CLIVAR Exchanges Special Issue* **56**, 15–19 (2011).
41. Leduc, G., Schneider, R., Kim, J.-H. & Lohmann, G. Holocene and Eemian sea surface temperature trends as revealed by alkenone and Mg/Ca paleothermometry. *Quat. Sci. Rev.* **29**, 989–1004 (2010).
42. Liu, Z. et al. The Holocene temperature conundrum. *Proc. Natl Acad. Sci. USA* **111**, E3501–E3505 (2014).
43. McKay, N. P., Kaufman, D. S., Routson, C. C., Erb, M. & Zander, P. D. The onset and rate of Holocene Neoglacial cooling in the Arctic. *Geophys. Res. Lett.* **45**, 487–496 (2018).
44. Harrison, S. P. et al. Evaluation of CMIP5 palaeo-simulations to improve climate projections. *Nat. Clim. Change* **5**, 735–743 (2015).
45. Bartlein, P. J., Harrison, S. P. & Kenji, I. Underlying causes of Eurasian midcontinental aridity in simulations of mid-Holocene climate. *Geophys. Res. Lett.* **44**, 9020–9028 (2017).
46. Ramisch, A. et al. A persistent northern boundary of Indian Summer Monsoon precipitation over Central Asia during the Holocene. *Sci. Rep.* **6**, 25791 (2016).

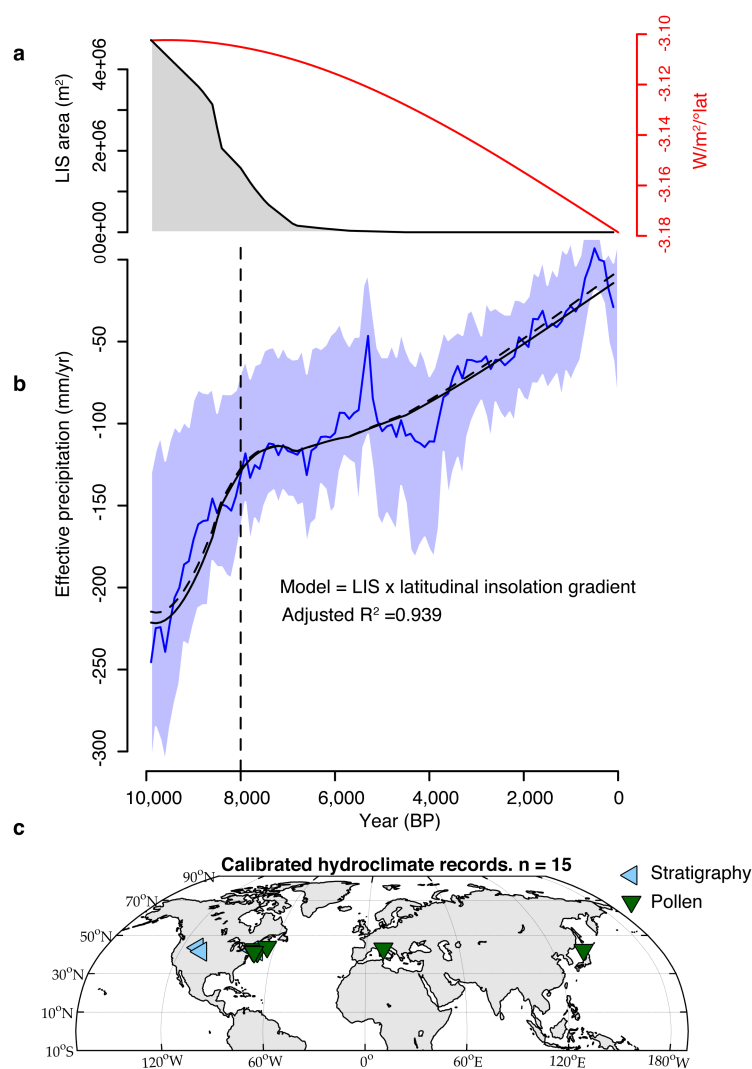


Extended Data Fig. 1 | Holocene insolation forcing by latitude and time. **a, b**, Change in (a) annual and (b) seasonal (JJA) insolation during the past 12,000 years caused by the Earth's orbital cycle. Values are anomalies

relative to present. Data from output of MATLAB code of ref. ³⁸, using the calendar days option and based on orbital parameters of ref. ¹⁴.



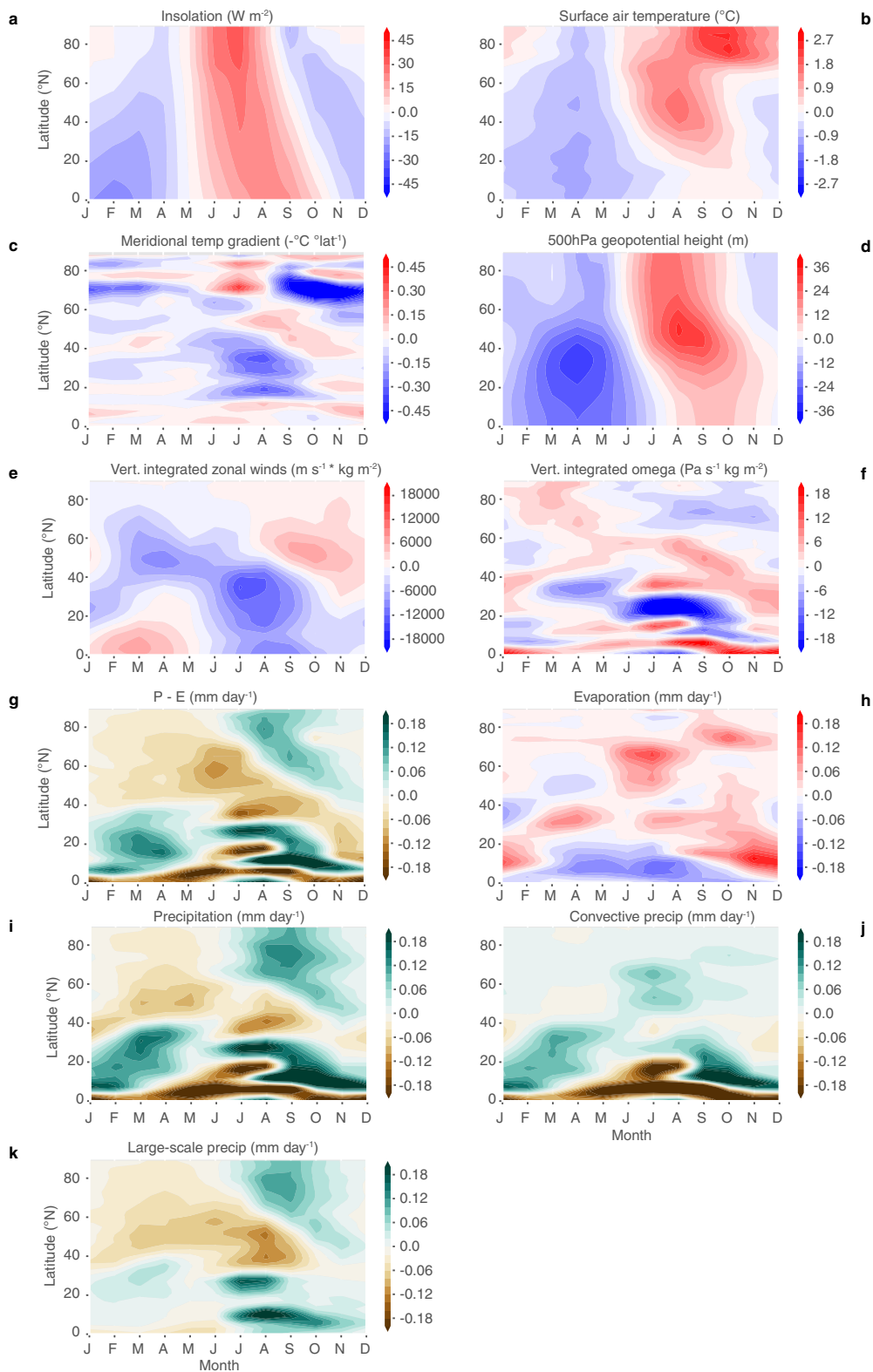
Extended Data Fig. 2 | Northern Hemisphere LTG at three temporal scales. **a–c,** Changes in LTG slope over (a) the instrumental period (twentieth century), (b) the past two millennia, and (c) Holocene (black) compared with Holocene annual latitudinal insolation gradient (red), and past two millennia LTGs binned to the same resolution as the Holocene data (dark blue). Gradients were calculated using linear regression across five 20° latitudinal composites as illustrated in Extended Data Fig. 8. Twentieth-century LTGs were calculated from CRU TS4.01 data¹⁵, last two millennia LTGs rely on the PAGES 2k network¹⁶, and Holocene-long LTGs use the new dataset presented in this study. Shading represents the one- and two-standard deviation bootstrapped confidence intervals over 500 iterations. Age and proxy temperature uncertainties included in the Holocene error estimations (Methods) smooth the error envelope with respect to the last two millennia, for which there is less age uncertainty¹⁶. The Holocene latitudinal insolation gradient uses data from ref. ¹⁴. The historical trend in **a** towards weaker gradients (less negative slopes) characterizes recent Arctic amplification.



Extended Data Fig. 3 | Calibrated hydroclimate records with insolation gradient and ice sheet area. **a**, Northern Hemisphere annual mean latitudinal insolation gradient¹⁴ and Laurentide Ice Sheet (LIS) area¹⁸. **b**, Calibrated hydroclimate records ($n = 15$, blue) with a fitted regression model using the annual insolation gradient and the LIS area. Shading represents the 95% bootstrapped uncertainty estimates (see Methods). Fitted dashed line is a simple linear model and the solid line includes an autoregressive (ar1) term for the residuals to account

for autocorrelation in the hydroclimate records. The fitted solid line indicates that the mean hydroclimate change represents an increase in net precipitation of $16.8 \pm 7 \text{ mm per } 0.01 \text{ W m}^{-2} \text{ per degree of latitude decrease in the annual insolation gradient since } 8 \text{ ka}$. Earlier amplification of the dryness in these records can probably be attributed to ice-sheet effects. **c**, Spatial distribution of calibrated hydroclimate records. The map was generated using code and associated data from ref. ³⁰.

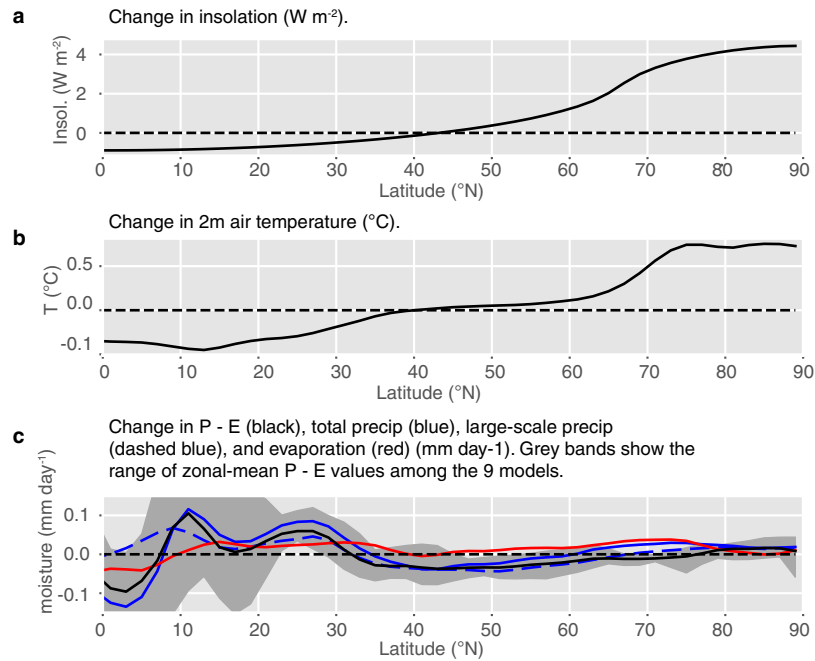
Change in zonal-mean quantities for MH-PI in a 9-model mean, all-points models: bcc-csm1-1, CCSM4, CNRM-CM5, CSIRO-Mk3-6-0, FGOALS-s2, IPSL-CM5A-LR, MIROC-ESM, MPI-ESM-P, MRI-CGCM3



Extended Data Fig. 4 | See next page for caption.

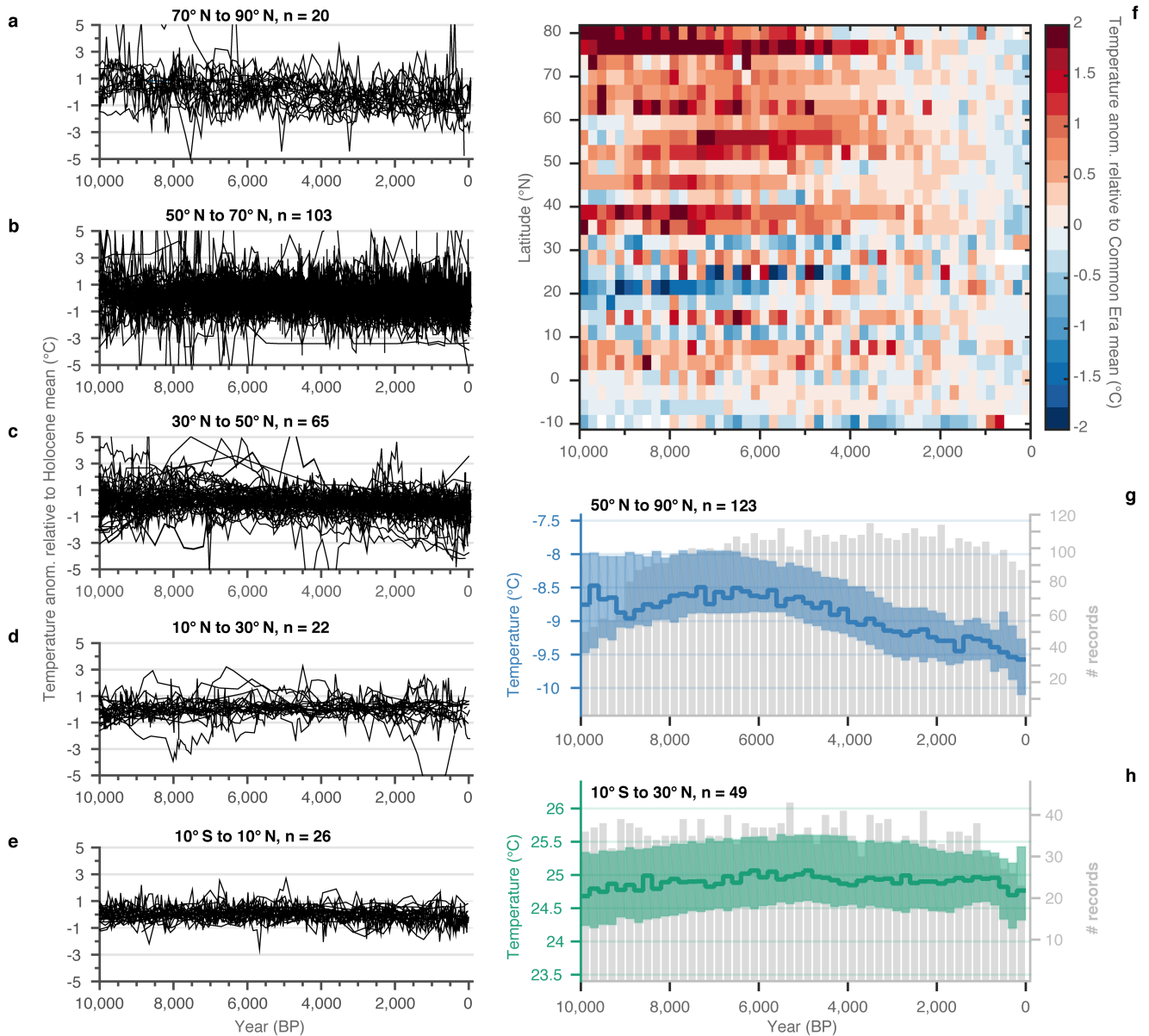
Extended Data Fig. 4 | Change in zonal-mean quantities for mid-Holocene (6 ka) minus preindustrial in a nine-model mean. Each panel is a Hovmöller figure showing zonal-mean climate anomalies by latitude (0° N to 90° N, y -axis) and calendar month (1–12, x -axis). **a**, The change in forcing is strongest in summer, and the insolation gradient change is weaker through much of the year. **b**, High-latitude warming anomalies dominate between June and December, with reductions in sea-ice extent likely to be causing the anomalous propagation of polar warmth into winter. **c**, The localized meridional temperature gradient anomalies (the derivative of temperature) shows weaker temperature gradients at 70° N between September and June. Negative values indicate a reduced temperature gradient. During summer (June through September) the temperature gradient anomaly is negative between 15° N and 50° N. **d**, Changes in 500 hPa geopotential height. **e**, Vertically integrated zonal

winds show reduced jet-stream strength for much of the year. **f**, Vertically integrated omega (vertical motion, with positive values indicating anomalous downward motion). **g**, Precipitation minus evaporation anomalies show decreases in mid-latitude net precipitation through much of the year. **h**, Evaporation. **i**, Total precipitation shows decreases in mid-latitude rainfall through much of the year. Large increases in localized total precipitation correspond to a shift in the intertropical convergence zone and increased monsoon strength. **j**, Convective precipitation shows enhanced monsoon systems. **k**, Large-scale precipitation (including extratropical cyclones) decreases from January through October, with the largest reductions in August. Vertically integrated quantities (**e**,**f**) are ‘mass-weighted’: the quantities are integrated on pressure levels from the surface to the top of atmosphere and divided by the standard gravity, then multiplied by -1 to give more easily interpretable quantities.



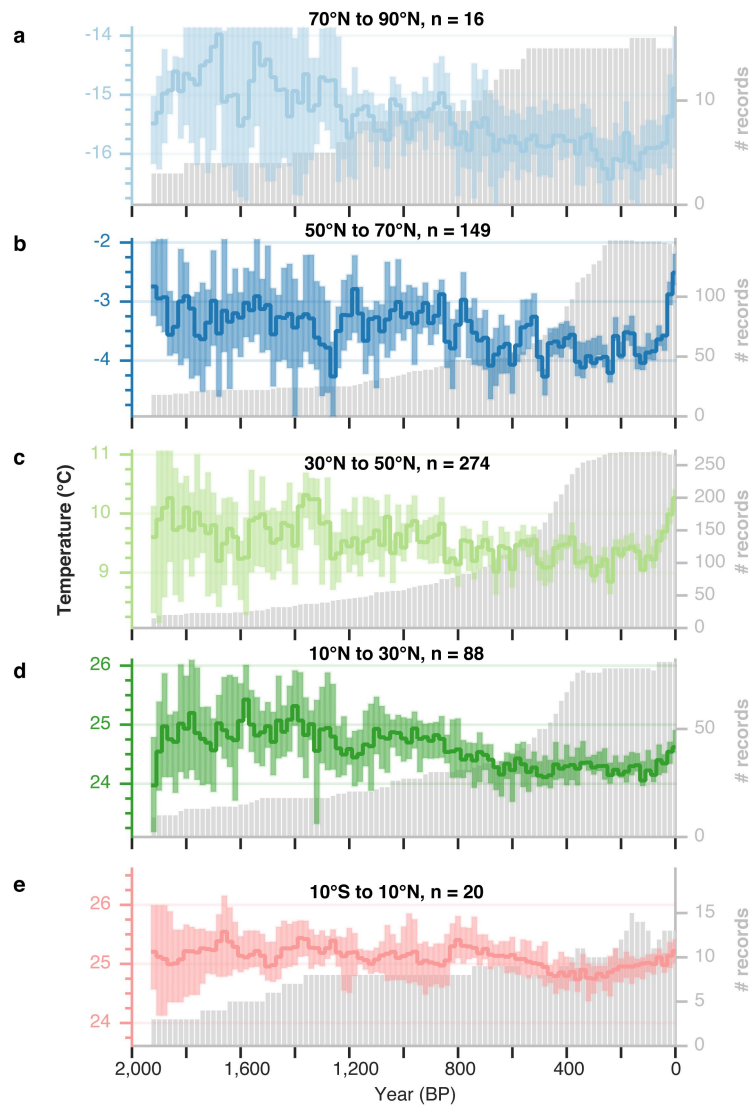
Extended Data Fig. 5 | PMIP3 model ensemble mid-Holocene minus preindustrial annual anomalies by latitude. a, Insolation anomalies showing decreased annual insolation at the Equator and enhanced insolation at the high latitudes. **b,** Temperature anomalies corresponding to the change in insolation. The higher temperatures at high latitudes and lower temperatures at low latitudes reduced the LTG at 6 ka by 0.011°C per degree of latitude, as calculated using the same procedures as for the proxy data. **c,** Changes in hydroclimate variables.

Precipitation (blue), large-scale precipitation (dashed blue), evaporation (red) and precipitation minus evaporation (black). The model spread for precipitation minus evaporation is shown in the grey band. Large positive and negative precipitation anomalies between 0°N and 30°N correspond to changes in monsoon strength and in the position of the intertropical convergence zone, which do not have strong agreement between models. Decreases in moisture between 30°N and $\sim 55^{\circ}\text{N}$ are smaller but consistent between models.



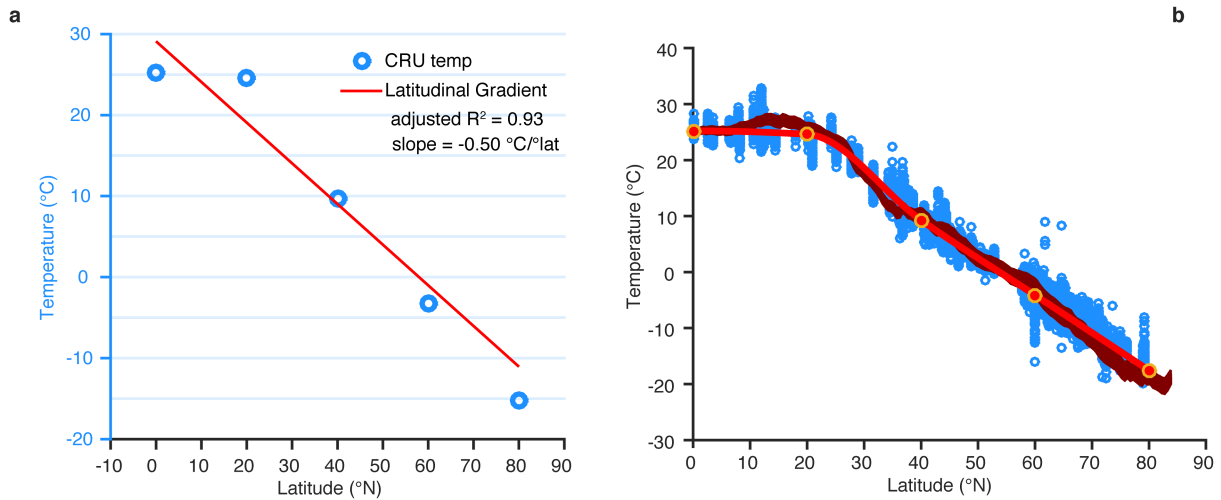
Extended Data Fig. 6 | Palaeo-temperature time series aggregated at different scales. a–e, All Holocene temperature records are adjusted to a mean of zero and subdivided by the latitudinal bands used to calculate the Northern Hemisphere LTG. To generate the temperature composites (Fig. 3a–e), median values were used to avoid the influence of the outliers visible here (some of the outliers extend beyond the y axis spanning 10 °C in a–e). **f,** A Hovmöller plot illustrating the evolution of Holocene temperature anomalies from the temperature proxy network binned into 5° latitudinal bands. The colour map is in temperature anomaly units of °C

with respect to the mean of 0 to 2,000 years BP. **g, h,** High-latitude (50° N to 90° N, **g**) and low-latitude (10° S to 30° N, **h**) temperature composites, with the number of contributing records in grey (200-year bins), and a y axis spanning 3 °C. Shading represents the 95% bootstrapped uncertainty estimate, which includes estimate of age and calibration uncertainties (Methods). The low-latitude composite was subtracted from the high-latitude composite as one of the three methods used to calculate the LTG shown in Fig. 3f.



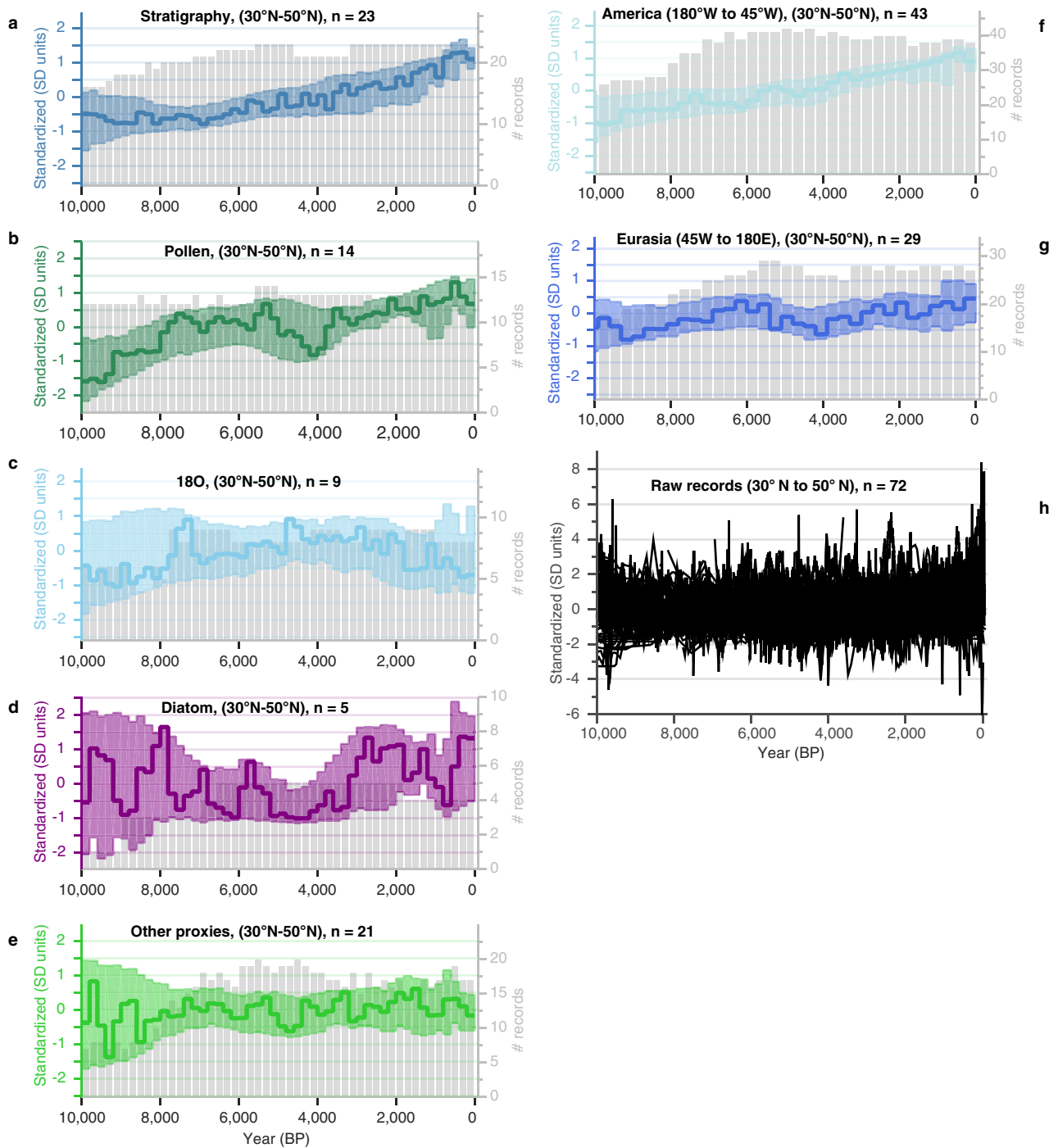
Extended Data Fig. 7 | Temperature composites spanning the last two millennia. a–e, The temperature composites represent five 20° latitudinal bands and were used to scale the Holocene composites shown in Fig. 3a–e. Time series are all displayed on the same scale, with each y-axis spanning

3 °C (left side). The number of contributing records to each composite are shown in grey (20-year bins) (right y-axis) (data from ref. ¹⁶). Shading denotes the bootstrapped sampling with replacement 95% confidence intervals.



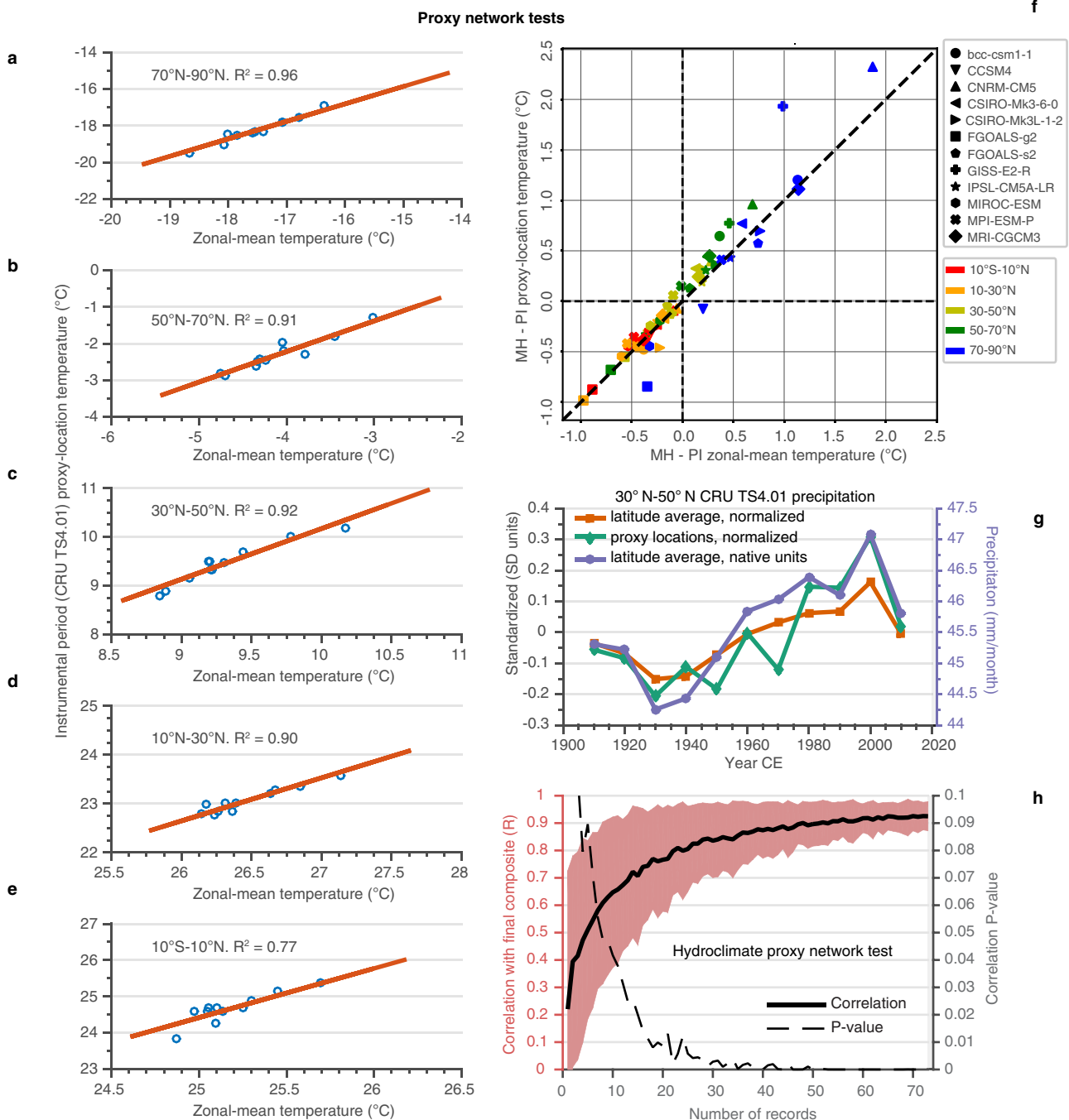
Extended Data Fig. 8 | Calculating the LTG. a, Average Equator-to-pole Northern Hemisphere LTG (red line) for the twentieth-century, calculated using CRU TS4.01 temperature data¹⁵ averaged across five latitude bands (blue symbols), and fit to robust linear regression, weighted by the cosine of latitude. **b,** LTG calculated using the second alternative method in which individual Holocene proxy records are scaled by latitude. CRU TS4.01¹⁵ temperature plotted by latitude in dark red. All the individual

years available in the CRU data are plotted as the resulting broad dark red line. The interpolated PAGES 2k network data¹⁶ used to scale the Holocene records are plotted in bright red, and mean temperatures for 100-year binned Holocene records are plotted as blue circles. The Holocene records were scaled by the period (500–1,500 BP) overlapping with the PAGES 2k dataset, which in turn was calibrated using the CRU TS4.01 data.



Extended Data Fig. 9 | Standardized Holocene hydroclimate proxy records from the mid-latitudes (30° N to 50° N). a–e, Time-series composites subdivided by dominant proxy types, with the number of contributing records in grey (200-year bins). Shading represents the 95% bootstrapped uncertainty estimate. f, g, Time-series composites by region. Mid-latitude (30° N to 50° N) hydroclimate in (f) North America (180° W to 45° W) and (g) Eurasia (45° W to 180° E) land area. North America was driest in the earliest Holocene (10 ka), with a gradual wetting trend to the present day. The Asian–European hydroclimate records suggest

that the driest conditions occurred during the early Holocene (10 ka to 8 ka). The Eurasian region had increasing net precipitation to about 6 ka, then decreasing net precipitation to about 4 ka, followed by increasing net precipitation to the present day. h, Individual hydroclimate records contributing to the mid-latitude (30° N to 50° N) composite (Fig. 3h), illustrating the variability among records across the mid-latitudes. All time series are standardized to have a mean of 0 and a standard deviation of 1 over the 0–10 ka interval. All y-axes are in standard deviation (SD) units.



Extended Data Fig. 10 | Proxy network sensitivity tests. **a–e**, Scatterplots showing the relation between decadal mean temperature at the proxy locations versus the average of the entire 20° latitudinal zone using gridded instrumental CRU TS4.01 temperature observations¹⁵. In the instrumental dataset, the mean temperature at the proxy locations explain between 77% and 96% of the variance in the latitudinal bands. The spread in data represents the overall temperature trend over the twentieth century. **f**, Mid-Holocene minus preindustrial (MH – PI) temperature averaged for the proxy locations (*y*-axis) versus the latitudinal averages (*x*-axis) from 12 PMIP3 climate models (symbols) across five latitudinal bands (colours). The models suggest that the proxy network captures the same mid-Holocene temperature anomalies as the latitudinal averages. **g**, Using gridded CRU TS4.01 precipitation observations¹⁵ to test the representativeness of the hydroclimate proxy network and the influence of standardization on the magnitude and variability in the composite time series. The standardized (mean = 0; variance = ± 1 s.d.) decadal

averaged composite is shown for the entire latitudinal zone 30° N to 50° N (orange squares) and for the proxy locations (green diamonds), along with the latitudinal average in native units (purple circles). The standardized mean from the proxy locations closely tracks the variability of the standardized and native unit latitudinal averages. **h**, Testing the number of proxy records needed to characterize Holocene hydroclimate changes in the mid-latitudes. Proxy record composites with iteratively smaller sample sizes were correlated with the final mid-latitude composite. The solid and dashed lines show the strength of correlation (*R* and *P* values, respectively) between the mid-latitude hydroclimate composite based on the full dataset of 72 records and composites using a randomly selected subset of fewer records. The error envelope shows the 95% bootstrapped random sampling confidence intervals. Correlation with the final composite begins to plateau near 40 records, suggesting our sample size of 72 is sufficient to represent the region.